


# PLANET: An Ellipse Fitting Approach for Simultaneous $T_1$ and $T_2$ Mapping Using Phase-Cycled Balanced Steady-State Free Precession

Yulia Shcherbakova <sup>1,\*</sup> Cornelis A.T. van den Berg,<sup>2</sup> Chrit T.W. Moonen,<sup>1</sup> and Lambertus W. Bartels<sup>1</sup>

**Purpose:** To demonstrate the feasibility of a novel, ellipse fitting approach, named PLANET, for simultaneous estimation of relaxation times  $T_1$  and  $T_2$  from a single 3D phase-cycled balanced steady-state free precession (bSSFP) sequence.

**Methods:** A method is presented in which the elliptical signal model is used to describe the phase-cycled bSSFP steady-state signal. The fitting of the model to the acquired data is reformulated into a linear convex problem, which is solved directly by a linear least squares method, specific to ellipses. Subsequently, the relaxation times  $T_1$  and  $T_2$ , the banding free magnitude, and the off-resonance are calculated from the fitting results.

**Results:** Maps of  $T_1$  and  $T_2$ , as well as an off-resonance and a banding free magnitude can be simultaneously, quickly, and robustly estimated from a single 3D phase-cycled bSSFP sequence. The feasibility of the method was demonstrated in a phantom and in the brain of healthy volunteers on a clinical MR scanner. The results were in good agreement for the phantom, but a systematic underestimation of  $T_1$  was observed in the brain.

**Conclusion:** The presented method allows for accurate mapping of relaxation times and off-resonance, and for the reconstruction of banding free magnitude images at realistic signal-to-noise ratios. **Magn Reson Med 79:711–722, 2018. © 2017 The Authors Magnetic Resonance in Medicine published by Wiley Periodicals, Inc. on behalf of International Society for Magnetic Resonance in Medicine. This is an open access article under the terms of the Creative Commons Attribution-NonCommercial-NoDerivs License, which permits use and distribution in any medium, provided the original work is properly cited, the use is non-commercial and no modifications or adaptations are made.**

**Key words:** ellipse fitting;  $T_1$ ;  $T_2$ ; off-resonance; phase-cycled bSSFP

## INTRODUCTION

Quantitative MR imaging plays an important role in accurate tissue characterization for improving clinical diagnostic imaging and for planning, guidance and evaluation of image-guided therapy. The mapping of longitudinal ( $T_1$ ) and transverse ( $T_2$ ) relaxation times is a particularly important tool for many clinical applications in oncology and regenerative medicine (1). Knowledge of  $T_1$  and  $T_2$  values allows optimizing the contrast-to-noise-ratio between tissues by finding the optimal sequence parameter settings.

Various techniques are widely used for  $T_1$  and  $T_2$  relaxation time mapping. 2D inversion recovery spin echo (IR-SE) and multi-echo spin echo (ME-SE) (2) are considered gold standard techniques, allowing accurate measurements of relaxation times. Unfortunately, scans based on these methods typically have a long acquisition time, which makes it challenging to use them in clinical practice. To speed up IR-based  $T_1$  mapping, the Look-Locker method was introduced (3). This approach is closely related to the IR-SE, but instead of acquiring a single image for each inversion time, the Look-Locker method uses an inversion pulse followed by a train of low flip angle (FA) pulses, each followed by a read-out, within each repetition time (TR). Although that considerably reduces the required scan time, it still is a time-consuming 2D method, which results in a very long acquisition time to cover a complete 3D volume.

Another widely used method, which uses the variable FA (VFA) approach (4,5), is DESPOT1 (6). The method allows for rapid 3D high-resolution  $T_1$  mapping and is easily implemented on clinical scanners. For this method, at least two acquisitions of spoiled gradient-echo (SPGR) scans with different FAs are required. A signal model for the steady-state is subsequently fitted to VFA data. A similar approach was developed by Deoni et al for  $T_2$  mapping under the name DESPOT2 and extended to the combined  $T_1$  and  $T_2$  mapping (7). DESPOT2 also requires at least two acquisitions of 3D balanced steady-state free precession (bSSFP) with different FAs using prior knowledge of  $T_1$ , often estimated using DESPOT1. Both methods have been shown error prone, which demands the optimization of the parameter settings. The combination of used FAs needs to be

<sup>1</sup>Center for Image Sciences, Imaging Division, University Medical Center Utrecht, Utrecht, The Netherlands.

<sup>2</sup>Department of Radiotherapy, Imaging Division, University Medical Center Utrecht, Utrecht, The Netherlands.

\*Correspondence to: Yulia Shcherbakova, M.Sc., Center for Image Sciences, Imaging Division, University Medical Center Utrecht, Heidelberglaan 100, Room Q.03.4.21, 3508 GA Utrecht, The Netherlands. E-mail: y.shcherbakova@umcutrecht.nl

This work is financed by the Netherlands Organisation for Scientific Research (NWO), grant 12813.

Received 19 September 2016; revised 23 March 2017; accepted 26 March 2017

DOI 10.1002/mrm.26717

Published online 22 May 2017 in Wiley Online Library (wileyonlinelibrary.com).

© 2017 The Authors Magnetic Resonance in Medicine published by Wiley Periodicals, Inc. on behalf of International Society for Magnetic Resonance in Medicine

This is an open access article under the terms of the Creative Commons Attribution-NonCommercial-NoDerivs License, which permits use and distribution in any medium, provided the original work is properly cited, the use is non-commercial and no modifications or adaptations are made.

optimized for improved accuracy and precision (8–10). Furthermore, the influence of radiofrequency field inhomogeneity (11), off-resonance effects (12,13), and radiofrequency and gradient spoiling efficiency (14,15) on the accuracy and precision of  $T_1$  and  $T_2$  measurements was investigated.

With the advent of stronger and faster gradient systems, bSSFP sequences have become widely used for rapid imaging with high signal-to-noise ratio (SNR) efficiency. Although the signal is a complex function of relaxation parameters  $T_1$  and  $T_2$ , several bSSFP-based approaches for relaxometry have been proposed, such as 2D inversion recovery TrueFISP (16), 3D triple echo steady-state (TESS) (17). For instance, the TESS method allows simultaneous rapid 3D estimation of  $T_1$  and  $T_2$  within one single scan using two specific signal ratios between three echoes (SSFP-FID and two SSFP-echo modes) and an iterative golden section search algorithm.

Generally, bSSFP imaging has a high sensitivity to local magnetic field inhomogeneities, which results in banding artifacts. Radiofrequency (RF) phase-cycled bSSFP imaging was introduced as a solution, and several algorithms were proposed to reduce banding artifacts (18).

Björk et al (19) introduced a parameter estimation algorithm to remove banding artifacts and simultaneously estimate relaxation times  $T_1$  and  $T_2$  from phase-cycled bSSFP. In their work, a combination of linear least squares fitting followed by a subsequent nonlinear iterative fitting was used, called the two step LORE-GN algorithm. They successfully reconstructed banding free magnitude images of a phantom and in vivo. Based only on simulations and numerical assessment of the Cramer-Rao Bound (CRB), they concluded that simultaneous estimation of  $T_1$  and  $T_2$  from phase-cycled bSSFP would be difficult at common SNR, because the CRB is high.

In this work, we introduce a novel approach, named PLANET, for simultaneous  $T_1$  and  $T_2$  estimation from phase-cycled bSSFP (20). The elliptical signal model is used to describe the phase-cycled bSSFP steady-state signal (21). The fitting of the model to the acquired data is reformulated into a linear convex problem, which is solved directly by a linear least squares method, specific to ellipses (22). Subsequently, the relaxation times  $T_1$  and  $T_2$  are analytically calculated from the fitting results.

Our work shows that accurate mapping of the relaxation times  $T_1$ ,  $T_2$ , the off-resonance caused by local field deviations, and banding free magnitude is feasible for realistic SNRs and can be performed with a regular coil setup and scan protocol parameter settings.

## METHODS

### Elliptical Signal Model

The elliptical signal model for bSSFP was first used by Xiang and Hoff (23) to remove banding artifacts. The complex bSSFP signal right after the RF pulse (at echo time  $t=0+$ ) can be described as:

$$I = M \frac{1 - ae^{i\theta}}{1 - b\cos\theta} \quad [1]$$

where

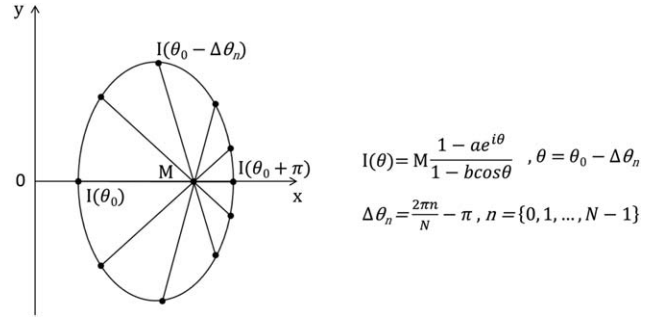


FIG. 1. The elliptical signal model of the bSSFP in the complex plane as a function of the resonance offset angle  $\theta$ . In this particular case,  $\theta_0 = 2\pi n$  and  $N = 10$  acquisitions with different RF phase increments are shown.

$$M = \frac{M_0(1 - E_1)\sin\alpha}{1 - E_1\cos\alpha - E_2^2(E_1 - \cos\alpha)}, a = E_2,$$

$$b = \frac{E_2(1 - E_1)(1 + \cos\alpha)}{1 - E_1\cos\alpha - E_2^2(E_1 - \cos\alpha)}$$

$E_1 = \exp\left(-\frac{TR}{T_1}\right)$ ,  $E_2 = \exp\left(-\frac{TR}{T_2}\right)$ ,  $M_0$  is the thermal equilibrium magnetization,  $\alpha$  is the FA, TR is the repetition time,  $\theta$  is the resonance offset angle (in radians),  $\theta = \theta_0 - \Delta\theta$ , where  $\theta_0 = 2\pi(\delta_{CS} + \Delta f_0)TR$ ,  $\Delta f_0$  is the off-resonance caused by local field deviations,  $\delta_{CS}$  is the chemical shift of the species (in Hz) with respect to the water peak,  $\Delta\theta$  is the user controlled RF phase increment (in radians). Parameters  $M$ ,  $a$ ,  $b$  are all  $\theta$ -independent.

Parametric Equation [1] describes an ellipse in the complex signal plane. Each point on the ellipse represents real and imaginary components of the transverse magnetization, which are acquired with a certain RF phase increment, as illustrated in Figure 1. The total number of acquisitions  $N$  and the RF phase increment  $\Delta\theta$  are user defined parameters.

Directly after the RF pulse (i.e., at  $t=0+$ ), the long axis of the ellipse is oriented vertically in the complex plane and the values for the parameters  $a$  and  $b$  are within the interval (0,1)(21). The cross-point  $M$  is the geometric solution (GS), which is independent of  $\theta$  and can be used to calculate a banding-free magnitude image.

At echo time  $t=TE > 0$  after the RF pulse, the signal is still a function of the resonance offset angle (21), but then the real and imaginary components of the signal are modulated by a factor  $\exp\left(-\frac{TE}{T_2}\right)$  and rotated around the origin by:

$$\varphi = \Omega TE = 2\pi(\delta_{CS} + \Delta f_0)TE \quad [3]$$

Taking into account the RF contribution, eddy current effects and  $B_0$  drift, the complex signal can be then described as:

$$I = M_{\text{eff}} \cdot \frac{1 - ae^{i\theta}}{1 - b\cos\theta} \cdot e^{i\varphi} \quad [4]$$

$$\varphi = 2\pi(\delta_{CS} + \Delta f_0)TE + \varphi_{RF} + \varphi_{\text{edd}} + \varphi_{\text{drift}} \quad [5]$$

where  $M_{\text{eff}} = KM \exp\left(-\frac{TE}{T_2}\right)$  is the effective magnetization,  $K$  is the magnitude of the combined receive field,

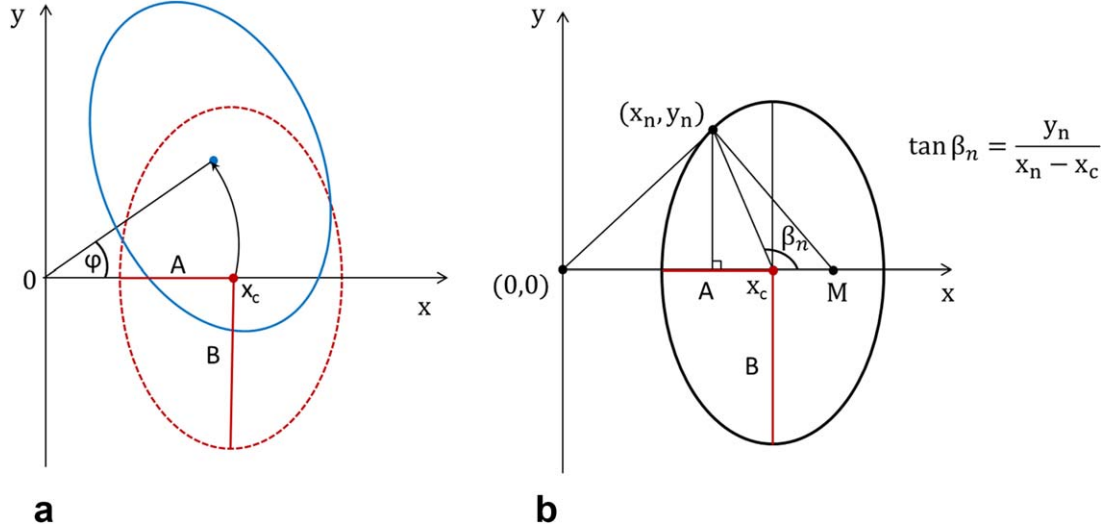


FIG. 2. **a**: Schematic representation of the ellipse at  $t=0+$  (red dashed line) and  $t=TE>0$  (blue solid line), which is rotated around the origin by  $\varphi$ .  $(x_c, 0)$  = the geometrical center of the ellipse;  $A, B$  = semi-axes of the ellipse. **b**: Geometrical determination of the angle  $\beta_n$  using the locations of the data points  $(x_n, y_n)$  on the vertical ellipse.

$\varphi_{RF}$  is the RF phase offset, related to the combination of RF transmit and receive phases,  $\varphi_{edd}$  is the extra phase errors due to eddy current effects, and  $\varphi_{drift}$  is the extra phase errors due to  $B_0$  drift.

#### Reconstruction Method for Parametric Mapping

Essential to the PLANET method is a three-step reconstruction algorithm to simultaneously estimate relaxation parameters  $T_1$  and  $T_2$ , and an effective banding free magnitude  $M_{\text{eff}}$  from phase-cycled bSSFP data. However, an additional step is required when the reconstruction of the off-resonance map  $\Delta f_0$  is also desired.

Step 1. Direct linear least squares ellipse fitting to phase-cycled bSSFP data.

The first step consists of performing voxel-wise direct linear least squares fitting of a general quadratic polynomial function to the data points in the complex plane (22):

$$F(\mathbf{C}, \mathbf{x}) = C_1 x^2 + C_2 xy + C_3 y^2 + C_4 x + C_5 y + C_6 = 0 \quad [6]$$

where  $x$  and  $y$  are real and imaginary components of transverse magnetization.

By minimizing the sum of squared algebraic distances of the ellipse to the data points under a proper scaling and an appropriate constraint specific to ellipses (discriminant  $C_2^2 - 4C_1C_3 = -1$ ), we avoid the trivial solution  $\mathbf{C} = \mathbf{0}$  and exclude all nonelliptical fits, such as hyperbola and parabola. As a result, we find a unique set of coefficients  $\mathbf{C} = [C_1, C_2, C_3, C_4, C_5, C_6]$  representing the ellipse. The fitting is based on a numerically stable version of the ellipse fit (24). This is a fast, direct, linear, non-iterative ellipse fit. Because there are six unknowns, we need at least six data points  $\mathbf{x}$ , which can be acquired by scanning with at least six different RF phase increment settings.

Step 2. Rotation of the ellipse to initial vertical conic form.

The rotation of data points of the ellipse to the initial vertical form, i.e., the orientation directly after RF

excitation pulse, was performed by applying basic algebraic transformations to the polynomial representation of the ellipse found in the previous step (Eq. [6]). We found the rotation angle  $\varphi_{rot}$  to be:

$$\varphi_{rot} = \frac{1}{2} \tan^{-1} \frac{C_2}{C_1 - C_3} \quad [7]$$

Because  $\varphi_{rot}$  is defined within  $(-\frac{\pi}{4}, \frac{\pi}{4})$ , we unwrapped it to cover the  $(-\pi, \pi)$  range by verifying that the ellipse of every voxel is vertical and that its center lies on the positive real axis.

After rotation, illustrated in Figure 2a, the conic equation for the vertical orientation can be used to describe the ellipse:

$$\frac{(x - x_c)^2}{A^2} + \frac{y^2}{B^2} = 1 \quad [8]$$

where  $(x_c, 0)$  is the geometrical center of the ellipse,  $A$  and  $B$  are the semi-axes of the ellipse.

Step 3. Analytical solution for parameters  $M_{\text{eff}}, T_1, T_2$ .

Parameters  $a, b, M_{\text{eff}}$  of the parametric form of the ellipse in Equation [4] are related to the geometric characteristics  $x_c, A, B$  from the Cartesian form of ellipse in Equation [8] through a system of nonlinear equations (23):

$$\begin{cases} x_c = M_{\text{eff}} \frac{1 - ab}{1 - b^2} \\ A = M_{\text{eff}} \frac{|a - b|}{1 - b^2} \\ B = M_{\text{eff}} \frac{a}{\sqrt{1 - b^2}} \end{cases} \quad [9]$$

We have solved this system for parameters  $a, b, M_{\text{eff}}$  analytically. The results are presented in the Appendix. The  $T_1$  and  $T_2$  estimates can be found from parameters  $a$  and  $b$  using the following equations:

$$T_1 = -\frac{TR}{\ln \frac{a(1 + \cos\alpha - abc\cos\alpha) - b}{a(1 + \cos\alpha - ab) - bc\cos\alpha}}; \quad T_2 = -\frac{TR}{\ln a} \quad [10]$$

Additional Step 4. Estimation of the local off-resonance  $\Delta f_0$ .

The rotation angle in Equation [7] includes the local off-resonance  $\Delta f_0 = \gamma\Delta B_0$  and RF phase offset  $\varphi_{RF}$ , which cannot be separated from Equation [5]. For simplicity, the chemical shift is ignored and the additional phase errors due to eddy current effects and  $B_0$  drift are assumed to be negligible:

$$\varphi_{rot} = 2\pi\Delta f_0 TE + \varphi_{RF} \quad [11]$$

The off-resonance  $\Delta f_0$ , however, can be estimated from the locations of the data points with different RF phase increment settings  $\Delta\theta_n$  on the vertical ellipse: the precession angle  $\theta_n$  during each TR depends only on the RF phase increment  $\Delta\theta_n$  and the local off-resonance  $\Delta f_0$ , and not on the RF phase offset  $\varphi_{RF}$ :

$$\theta_n = \theta_0 - \Delta\theta_n = 2\pi TR\Delta f_0 - \Delta\theta_n \quad [12]$$

Using a Cartesian parametric equation of the ellipse:

$$\begin{cases} x = x_c + A\cos t \\ y = B\sin t \end{cases}, \quad \text{where } t = \tan^{-1}\left(\frac{A}{B}\tan\beta\right) \quad [13]$$

and after substitution of  $x$  and  $y$  from Equation [13] by the real and imaginary components of the signal in Equation [4], the relationship between parameters  $t$  and  $\theta$  can be found as:

$$\cos\theta = \frac{\cos t - b}{b\cos t - 1} \quad [14]$$

For each individual  $n^{\text{th}}$  data point with  $n = \{0, 1, \dots, N-1\}$  Eq. [14] is equivalent to

$$\cos\theta_n = \frac{\cos t_n - b}{b\cos t_n - 1} \quad [15]$$

The set of  $t_n$  can be found from the set of  $\beta_n$  using Equation [13]. The set of  $\beta_n$  can be found geometrically from the data points on the vertical ellipse as illustrated in Figure 2b and consequently, the set of  $\cos\theta_n$  can be found from Equation [15] and can be represented by the sum of a sine function and a cosine function:  $\cos(\theta_n) = \cos(\theta_0 - \Delta\theta_n) = \cos\theta_0\cos\Delta\theta_n + \sin\theta_0\sin\Delta\theta_n = K_1\cos\Delta\theta_n + K_2\sin\Delta\theta_n$ .

Next, the coefficients  $K_1$  and  $K_2$  can be found by taking a linear least squares fitting approach and  $\theta_0$  can be estimated from:

$$\theta_0 = \tan^{-1}\frac{K_2}{K_1} \quad [16]$$

The off-resonance  $\Delta f_0$  can be found from Equations [12] and [16]. Because  $\theta_0$  is defined within  $(-\pi, \pi)$ , we unwrapped it to cover the range  $(-2\pi, 2\pi)$ , which results in a bandwidth  $(-\frac{1}{TR}, \frac{1}{TR})$ .

### Sensitivity to FA Errors

To investigate how sensitive the method is to errors in the actual FA, simulations were performed for a range of

nominal FAs between  $1^\circ$  and  $90^\circ$  and a range of deviation in actual FAs of  $-10\%$  and  $+10\%$ . The initial parameter settings were:  $KM_0 = 1$ ,  $T_1 = 675$  ms,  $T_2 = 75$  ms,  $\Delta f_0 = 10$  Hz,  $TR = 10$  ms,  $TE = 5$  ms,  $\varphi_{RF} = 0$ ,  $\delta_{CS} = 0$ ,  $N = 10$  phase cycles with phase increments  $\Delta\theta_n = \frac{2\pi n}{N} - \pi$ ,  $n = \{0, 1, \dots, 9\}$ . The chosen  $T_1$  and  $T_2$  represent white matter at 1.5T. No Gaussian noise was added.

### Experimental Validation

To investigate the performance of our method, both phantom and human volunteer experiments were performed on a clinical 1.5T MR scanner (Philips Ingenia, Best, The Netherlands). For all scans, a 16-channel head coil (dS HeadSpine, Philips Ingenia, Best, The Netherlands) was used as a receive coil.

The phantom experiments were performed on a calibrated phantom consisting of gel tubes with known  $T_1$  and  $T_2$  values (TO5, Eurospin II test system, Scotland). Twelve tubes were chosen with  $T_1$ ,  $T_2$  combinations in the following ranges:  $T_1$  (220–1600 ms),  $T_2$  (50–360 ms).

First, the known temperature dependence of the relaxation times of the calibrated gels was used to assess the  $T_1$  and  $T_2$  values of the test tubes for the actual scanner room temperature. The temperature inside the phantom water was measured before and right after the experiment using a T-type thermocouple. The difference between measured temperature values was below  $0.5^\circ$  and the average value was chosen for the correction.

The 3D phase-cycled bSSFP sequence was performed with the protocol parameter settings, shown in Table 1. Complex-valued data were acquired.

Reference  $T_1$  and  $T_2$  maps of the phantom were acquired using standard  $T_1$  and  $T_2$  mapping techniques. For the reference  $T_1$  mapping, a 2D turbo IR-SE approach was used. For the reference  $T_2$  map, a 2D ME-SE approach was used. The corresponding protocol parameter settings are shown in Table 1. A reference off-resonance map was calculated using a dual echo SPGR method with the protocol parameter settings shown in Table 1.

Before voxel-wise parameter estimation, all images were masked to exclude the borders of the tubes and the background from the analysis.

The reference  $T_1$  values were calculated voxel-wise by performing the nonlinear fit of  $S(TI) = \rho|1 - 2e^{-TI/\tau_1}|$  to multi TI IR-SE data, with  $\rho$  and  $T_1$  as the fitting parameters. The reference  $T_2$  values were calculated voxel-wise by performing the nonlinear fit of  $S(TE) = \rho e^{-TE/\tau_2}$  to ME-SE data, with  $\rho$  and  $T_2$  as the fitting parameters.

To demonstrate the method in vivo, experiments were performed on the brain of three healthy volunteers on the same scanner. The protocol parameter settings for 3D phase-cycled bSSFP are presented in Table 1. As shown in the Appendix, the FA should fulfill the condition  $FA > \cos^{-1}\left(\exp\left(-\frac{TR}{T_1 \text{ shortest}}\right)\right)$ . Thus, FA  $30^\circ$  was used, which should allow an accurate estimation from  $T_1 > 100$  ms onward for  $TR = 10$  ms.

The reference  $T_1$  and  $T_2$  values of the brain were measured using a simultaneous (interleaved) spin echo and inversion recovery method (2D MIXED) (25) with the protocol parameter settings, shown in Table 1.

Table 1  
Protocol Parameter Settings

Phantom experiments 3D phase-cycled bSSFP									
FOV (mm <sup>3</sup> )	Voxel size (mm <sup>3</sup> )	Acq. matrix	TR (ms)	TE (ms)	FA (°)	Number of RF increment steps	NSA	Readout direction	Total scan time (min:s)
200x200x80	1.5x1.5x2.5	132x132x32	10	5	30	10	1	AP	06:51
Reference $T_1$ map (2D IR-TSE)									
FOV (mm <sup>3</sup> )	Voxel size (mm <sup>3</sup> )	Acq. matrix	TR (ms)	TE (ms)	Turbo factor	Inversion times (ms)	NSA	Readout direction	Total scan time (min:s)
200x200x5	2.5x2.5x5	80x80x1	7000	10	5	[25; 50; 100; 200; 500; 1000; 2000; 5000]	1	AP	16:00
Reference $T_2$ map (2D ME-SE)									
FOV (mm <sup>3</sup> )	Voxel size (mm <sup>3</sup> )	Acq. matrix	TR (ms)	TE (ms)	NSA	Readout direction	Total scan time (min:s)		
200x200x5	2.5x2.5x5	80x80x1	5000	[20; 40; 60; 80; 100; 120; 140; 160]	1	AP	06:45		
Reference off-resonance map (3D dual echo SPGR)									
FOV (mm <sup>3</sup> )	Voxel size (mm <sup>3</sup> )	Acq. matrix	TR (ms)	TE (ms)	FA (°)	NSA	Readout direction	Total scan time (min:s)	
200x200x80	2x2x2.5	100x100x32	30	[4.6; 9.2]	60	1	AP	03:08	
In vivo experiments 3D phase-cycled bSSFP									
FOV (mm <sup>3</sup> )	Voxel size (mm <sup>3</sup> )	Acq. matrix	TR (ms)	TE (ms)	FA (°)	Number of RF increment steps	NSA	Readout direction	Total scan time (min:s)
220x220x100	1.5x1.5x4	148x148x25	10	5	30	10	1	AP	06:04
Reference $T_1$ and $T_2$ map (2D MIXED)									
FOV (mm <sup>3</sup> )	Voxel size (mm <sup>3</sup> )	Acq. matrix	TR SE (ms)	TR IR (ms)	IR delay (ms)	TE (ms)	NSA	Readout direction	Total scan time (min:s)
220x220x4	1.5x1.5x4	148x148x1	3000	6000	500	[30; 60; 90; 120; 150; 80; 210; 240]	1	AP	16:00
B <sub>1</sub> map (3D dual TR SPGR)									
FOV (mm <sup>3</sup> )	Voxel size (mm <sup>3</sup> )	Acq. matrix	TR (ms)	TE (ms)	FA (°)	NSA	Overcontiguous slice	Readout direction	Total scan time (min:s)
220x220x100	2.5x2.5x4	88x88x25	[30; 150]	2.1	60	1	Yes	AP	03:17

NSA = Number of signal averages.

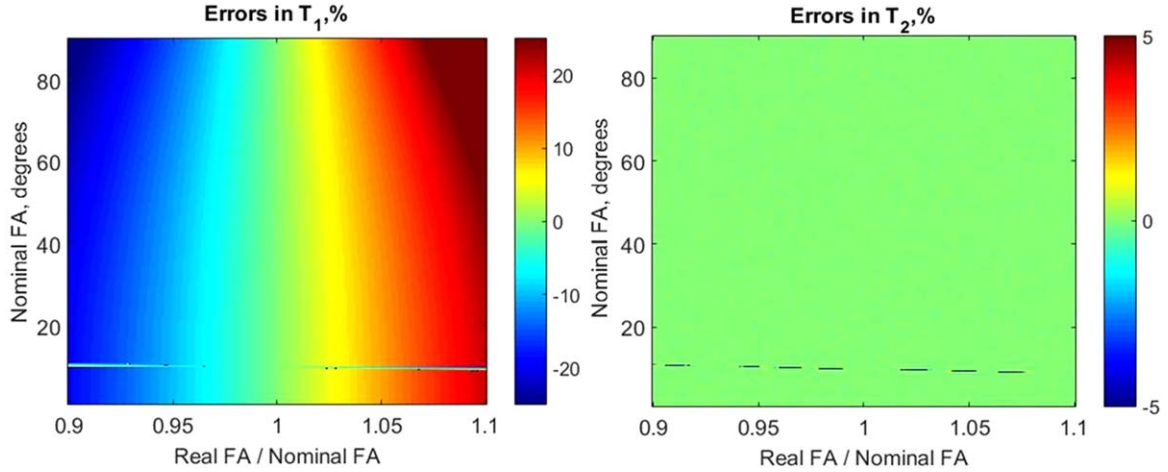


FIG. 3. Simulation results of sensitivity to the actual FA errors. The initial  $T_1 = 675$  ms,  $T_2 = 75$  ms,  $TR = 10$  ms,  $TE = 5$  ms. The horizontal line corresponds to the nominal  $FA = 10^\circ$ , which leads to collapsing of the ellipse to a line, as discussed in the Appendix.

$B_1$  map was calculated using a dual TR actual FA imaging (26) method with the protocol parameter settings, presented in Table 1.  $B_1$  correction was performed voxel-wise for the calculated  $T_1$  maps.

To investigate an influence of magnetization transfer (MT) effects on the quantitative  $T_1$  and  $T_2$  mapping in vivo, experiments were performed on one volunteer using 3D phase-cycled bSSFP with different RF excitation pulse durations, as suggested in work by Bieri and Scheffler (27). The protocol parameter settings were the same as shown in Table 1 (3D phase-cycled bSSFP in vivo). The default pulse had a duration 0.84 ms. The long pulse optimized to minimize the MT effects had a duration 2.86 ms.

The signal ratio  $\Delta S$  and MT ratio (MTR) were calculated as:  $\Delta S = \frac{M_{\text{def}}}{M_0}$ ,  $MTR = 100 \frac{M_0 - M_{\text{def}}}{M_0}$ , where  $M_{\text{def}}$  is the banding free magnitude measured with the default RF pulse,  $M_0$  is the banding free magnitude measured with the long RF pulse (minimized MT effects).

A linear phase-encoding profile order was used to minimize the eddy currents induced by changing phase-encoding gradients (28).

The standard (fast channel combination) method, available on the scanner, was used for the combined phase reconstruction. Note that the RF phase offset  $\varphi_{RF}$  remains the same for all dynamics with different RF phase increments settings.

To check the amount of  $B_0$  field drift, one additional dataset with RF phase increment  $\Delta\theta_{RF} = \pi$  was usually acquired at the end of the acquisition. In case of absence of  $B_0$  drift during the acquisition, the complex signals should be the same for data with  $\Delta\theta_{RF} = -\pi$  and  $\Delta\theta_{RF} = \pi$ , otherwise the phase difference between these datasets is proportional to the amount of the drift.

The SNR for both phantom and in vivo data was calculated as defined in the work by Björk et al (19):

$$SNR = \frac{\sum_{n=1}^N |I_n(\theta)|}{N\sigma} \quad [17]$$

where  $|I_n(\theta)|$  is the magnitude of  $n^{\text{th}}$  phase-cycled image,  $\sigma$  is the standard deviation of noise,  $N$  is number of

scans with different RF phase increment settings. The standard deviation of noise was calculated over the region of interest (ROI) on noise images (real and imaginary components), acquired dynamically using the same bSSFP sequence, without RF excitation and with no gradients applied.

All simulations and calculations were performed in MATLAB R2015a (The MathWorks Inc, Natick, MA).

## RESULTS

### Sensitivity to the Actual FA Errors

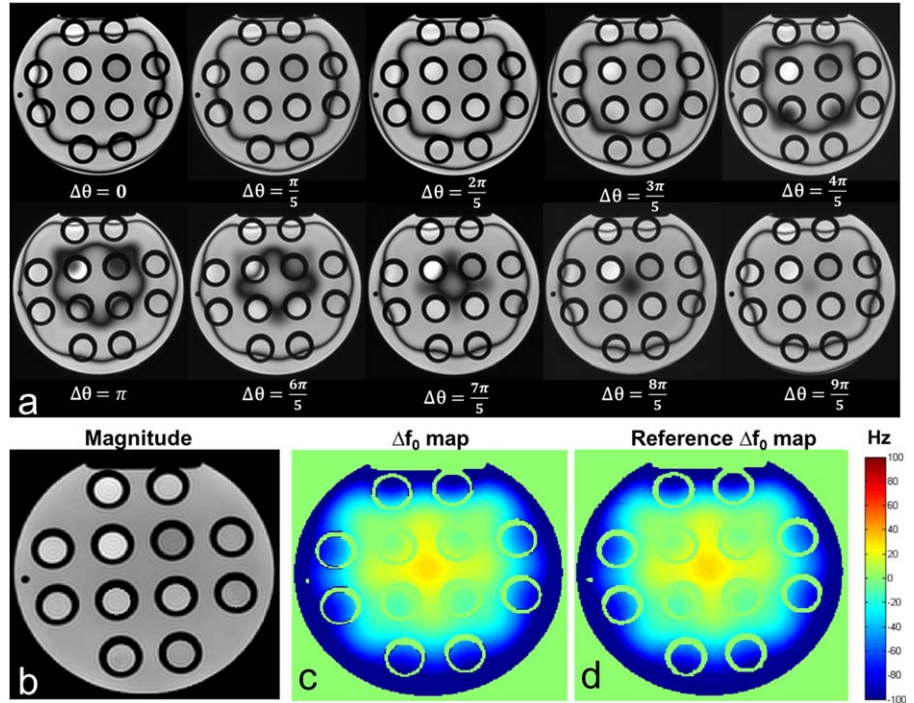
As can be observed from Figure 3,  $T_1$  estimates are highly sensitive to errors of the actual FA. The dependence is almost linear and the errors in  $T_1$  estimates increase with increasing FA. For example, 5% error (0.95) in actual FA results in 10% underestimation in  $T_1$  for the nominal FA of  $30^\circ$  and 12% underestimation in  $T_1$  for the nominal FA of  $60^\circ$ .  $T_2$  estimates are not affected by the errors in actual FA.

### Phantom Results

$T_1$ ,  $T_2$ , and  $\Delta f_0$  maps were first validated in a phantom magnitude images corresponding to different RF phase increment settings are presented in Figure 4a. The banding artifacts, the locations of which depend on the resonance offset angle, are shifted depending on the RF phase increment setting. The GS, representing the banding-free effective magnitude image, was calculated for a set of acquired data and is presented in Figure 4b. The off-resonance maps of the phantom were calculated using the PLANET method and using the reference method. The results are presented in Figures 4c,d. The two off-resonance maps look almost similar. A minor deviation between the two calculated maps of  $[-2; +1]$  Hz was observed.

$T_1$  and  $T_2$  maps of the phantom were calculated using the PLANET method and using the reference methods. The results are presented in Figure 5. The processing time for the reconstruction of  $T_1$ ,  $T_2$ ,  $\Delta f_0$  and banding-free effective magnitude  $M_{\text{eff}}$  for one slice

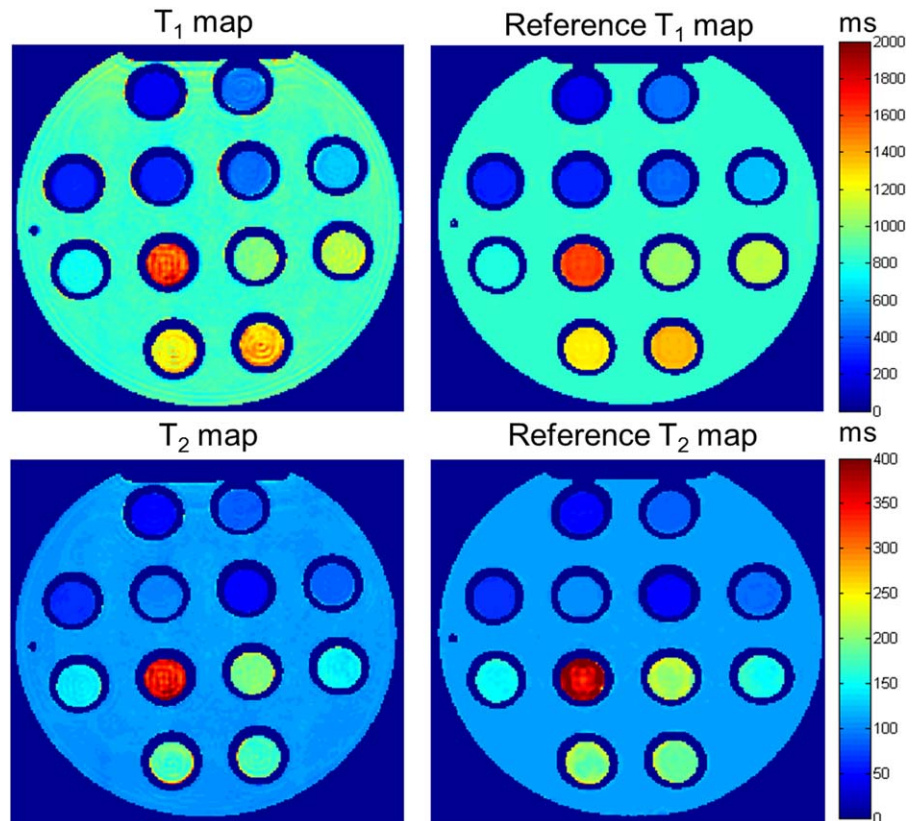
FIG. 4. **a**: Magnitude images corresponding to different RF phase increments setting  $\Delta\theta$ . **b**: The banding-free effective magnitude. **c,d**: The off-resonance maps calculated using the PLANET method and using the reference method.



was 6 s. We generally see a good quantitative agreement between reference and calculated from the PLANET method maps. However, there are some inhomogeneous regions inside some of the phantom tubes. The comparisons between the average  $T_1$  and  $T_2$  values

for each of the phantom tubes are shown in Figure 6. Standard deviations in  $T_1$  and  $T_2$  were calculated for each tube. The estimated accuracy of tabulated  $T_1$  and  $T_2$  values of the test object, provided by the manufacturer, is  $\pm 3\%$ .

FIG. 5. Experimental results from the phantom study:  $T_1$  and  $T_2$  maps calculated using the PLANET method and using the reference method.



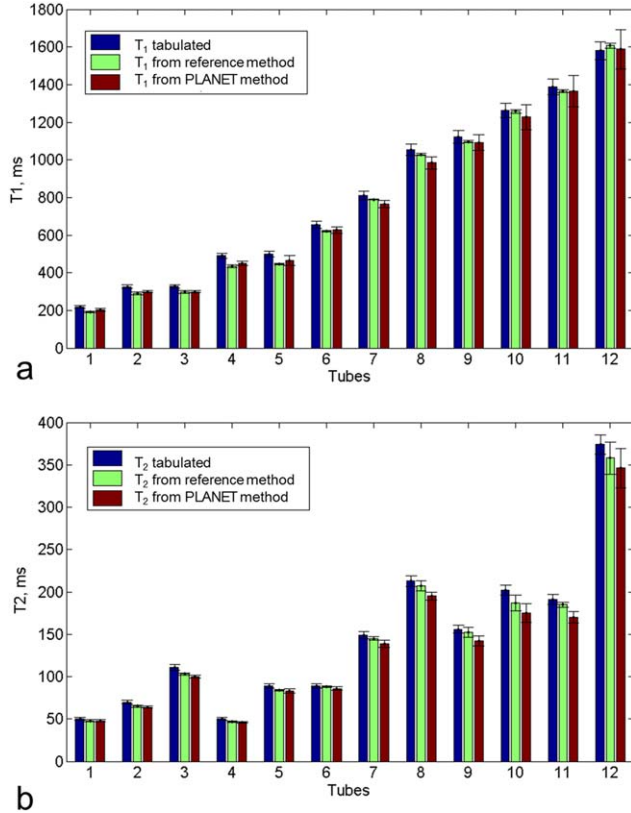


FIG. 6. Experimental results from the phantom study: comparison between average  $T_1$  (a) and  $T_2$  (b) values for the phantom tubes: blue = the tabulated values, green = calculated from the reference methods, red = calculated from the PLANET method. The mean  $T_1$  and  $T_2$  values of the gels were calculated for one slice in the center of the phantom by averaging over an ROI (around 250 voxels) inside each tube on estimated  $T_1$  and  $T_2$  maps. Precision of  $T_1$  and  $T_2$  measurement was evaluated by calculating standard deviations on estimated  $T_1$  and  $T_2$  maps over the same ROIs.

### Results In Vivo

Figures 7a,b show the reference  $T_1$  and  $T_2$  maps of one axial slice of the brain of a healthy volunteer. The results of measurements in three different axial slices through the brain are shown in Figures 7c–f. The banding free effective magnitude is presented, as well as the  $T_1$  and  $T_2$  maps calculated using the PLANET method. The off-resonance maps were calculated using the PLANET method and using the reference method. The minor observed deviation between the off-resonance maps was  $[-3;+3]$  Hz. The processing time for the reconstruction of  $T_1$ ,  $T_2$ ,  $\Delta f_0$ , and  $M_{\text{eff}}$  for one slice was 7 s. On the  $T_1$  and  $T_2$  maps a good contrast between gray matter (GM), white matter (WM), and cerebrospinal fluid (CSF) can be seen. The calculated mean  $T_1$  and  $T_2$  for WM and GM after  $B_1$  correction are presented in Table 2 in comparison with the reference values and those published in literature (7,29).

An underestimation in  $T_1$  by approximately 15–20% in WM and GM compared with the reference values was observed.  $T_2$  values in WM were underestimated by approximately 10% compared with the reference values,  $T_2$  values in GM were determined very precisely compared with the reference values.

Examples of the acquired complex signals for WM, GM, and CSF with the corresponding elliptical fits are shown in Figure 8. The orientation of three ellipses is different, which is explained by difference in off-resonance for those voxels.

$T_1$  and  $T_2$  maps, calculated from datasets, acquired using the default and long RF excitation pulses, as well as signal ratio and MTR are presented in Supporting Figure S1, which is available online. The quantitative results from three ROIs placed in WM are shown in Supporting Table S1. The average relative signal loss due to MT effects in WM was found to be 13% and the average  $T_1$  shortening was 8%. The estimated SNR maps of the phantom and the brain are presented in Supporting Figure S2.

We did not observe any significant  $B_0$  drift between acquisitions with increments  $\Delta\theta_{\text{RF}} = -\pi$  and  $\Delta\theta_{\text{RF}} = \pi$ , which were performed at the start and at the end of sequence. The maximum phase difference between these datasets was 0.04 rad for the phantom and 0.06 rad for the brain experiment.

### DISCUSSION

The fitting of the elliptical signal model is a very important aspect of the proposed PLANET method. We reformulated the fitting procedure into a linear convex problem, which can be solved directly by using a linear least-squares method. Prior knowledge of the elliptical trajectory in the complex plane allows to reduce the solution space to one unique solution by applying a proper scaling and an ellipse-specific constraint. In combination with analytical solutions for parameters  $T_1$ ,  $T_2$ , and  $M_{\text{eff}}$ , which take the fitting results as input, our approach becomes simple, robust, and fast. This is a clear advantage of our method compared with all iterative algorithms, which usually have longer reconstruction time and fitting problems related to local minima. The whole reconstruction time is very fast, which facilitates the adoption of the proposed method into clinical practice.

Compared with the work by Björk et al (19), who used a combination of linear fitting followed by subsequent nonlinear fitting and only four phase-cycled acquisitions, the PLANET method requires at least six phase-cycled acquisitions to directly fit the model to the experimental data. The inclusion of prior knowledge of the elliptical trajectory is essential and differs clearly from the methodology followed by Björk et al. Contrary to their conclusions, which were based only on simulations, that the simultaneous  $T_1$  and  $T_2$  estimation using their algorithm is not feasible for realistic SNRs, we experimentally demonstrated that it is feasible to use the PLANET method at realistic SNRs, both in a phantom and in vivo, with a regular coil setup and protocol parameters settings.

The reported values of  $T_1$  and  $T_2$  in the phantom are in good agreement with the calibrated values and those calculated with reference methods. However, in some of tubes some inhomogeneous regions in the form of "ghosts" near the tube borders are observed in the resultant  $T_1$  and  $T_2$  maps of the phantom, which leads to an underestimation of the calculated  $T_1$  and  $T_2$  values for those tubes.



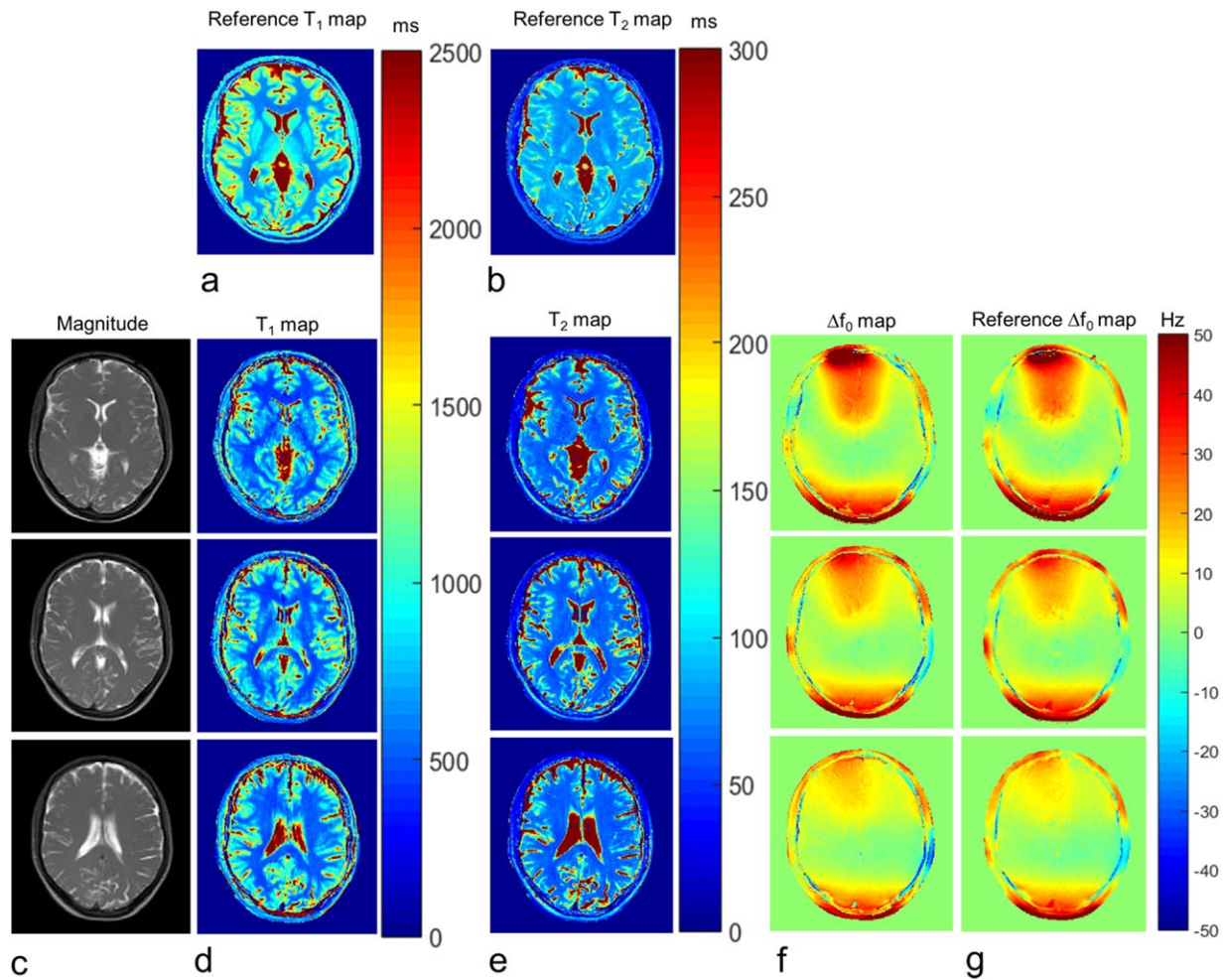


FIG. 7. Experimental results from the volunteer study:  $T_1$  map for one axial slice of the brain calculated using the reference method (a);  $T_2$  map for one axial slice of the brain calculated using the reference method (b); the banding free effective magnitude images (c);  $T_1$  maps calculated using the PLANET method (d);  $T_2$  maps calculated using the PLANET method (e); the off-resonance maps calculated using the PLANET method (f); the off-resonance maps calculated using the reference method (g). The position of the axial slice (a,b) is different from the positions of slices (c-g).

Table 2  
Results from In Vivo Experiment:  $T_1$  and  $T_2$  Values Determined Using the PLANET Method and Using the Reference Method Compared With Published Values<sup>a</sup>

PLANET					Reference 2D MIXED method									
ROI #	White matter		Gray matter		ROI #	White matter		Gray matter						
	$T_1$ (ms)	$T_2$ (ms)	$T_1$ (ms)	$T_2$ (ms)		$T_1$ (ms)	$T_2$ (ms)	$T_1$ (ms)	$T_2$ (ms)					
1	461 ± 19	62 ± 2	754 ± 47	80 ± 2	1	636 ± 15	75 ± 2	1016 ± 53	84 ± 3					
2	466 ± 25	61 ± 2	749 ± 75	84 ± 8	2	602 ± 14	75 ± 2	1014 ± 30	82 ± 4					
3	453 ± 15	62 ± 2	836 ± 70	83 ± 5	3	597 ± 13	73 ± 2	999 ± 52	84 ± 2					
4	524 ± 19	64 ± 2	876 ± 71	82 ± 4	Mean	612 ± 14	74 ± 2	1010 ± 46	83 ± 3					
5	512 ± 30	64 ± 2	837 ± 67	80 ± 4	Literature published values <sup>a</sup>									
6	525 ± 18	63 ± 2	787 ± 24	98 ± 9	Ref <sup>b</sup>	$T_1$ (ms)	$T_2$ (ms)	$T_1$ (ms)	$T_2$ (ms)					
7	528 ± 22	64 ± 3	906 ± 48	90 ± 14										
8			789 ± 24	84 ± 4						Ref IR;SE (7)	615 ± 12	69 ± 2	1002 ± 56	92 ± 3
9			787 ± 24	84 ± 4						Ref (7)	621 ± 61	58 ± 4	1060 ± 133	98 ± 7
Mean	496 ± 22	63 ± 2	813 ± 54	85 ± 5	Ref (29)	561 ± 12	73 ± 2	1048 ± 61	94 ± 6					

<sup>a</sup>The mean  $T_1$  and  $T_2$  values of WM were calculated for five slices of the brain by averaging over seven ROIs (each around 100 voxels) in WM on estimated  $T_1$  and  $T_2$  maps. The reference mean  $T_1$  and  $T_2$  values of WM were calculated for one slice of the brain by averaging over three ROIs (each around 100 voxels) in WM on the reference  $T_1$  and  $T_2$  maps. The mean  $T_1$  and  $T_2$  values of GM were calculated for five slices of the brain by averaging over nine ROIs (each around 30 voxels) in GM on estimated  $T_1$  and  $T_2$  maps. The reference mean  $T_1$  and  $T_2$  values of GM were calculated for one slice of the brain by averaging over three ROIs (each around 30 voxels) in GM on the reference  $T_1$  and  $T_2$  maps. The precision of  $T_1$  and  $T_2$  measurement was evaluated by calculating standard deviations on estimated  $T_1$  and  $T_2$  maps over the same ROIs.

<sup>b</sup>Numbers in parentheses are reference citations.

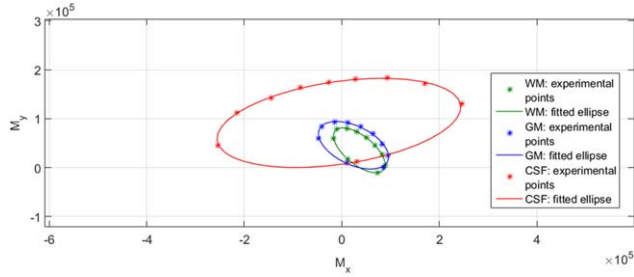


FIG. 8. Examples of the acquired complex signals for white matter, gray matter, and CSF with the corresponding elliptical fits from three voxels of the brain of a healthy volunteer.

This effect may have been caused by Gibbs ringing artifacts. The influence of these artifacts on estimated  $T_1$  maps needs to be further investigated and minimized.

$T_1$  and  $T_2$  maps obtained in the brain of volunteers were generally in agreement with the reference maps and values in literature (7,29); however, the  $T_1$  values were underestimated.  $B_1$  field inhomogeneities, resulting in errors in the actual FA, have shown a significant influence on the estimated  $T_1$  values. The errors caused by this effect depend on the used FA and were corrected using additionally acquired  $B_1$  maps. Unlike  $T_1$  estimates,  $T_2$  estimates were not affected by the errors in actual FA. MT effects were shown to have an influence on  $T_1$  quantification, particularly in WM. A partial mitigation strategy to minimize the impact of MT effects, as proposed by Bieri et al, was to use long RF excitation pulses in a combination with relatively low FA and long TR. Note that effects related to the presence of deoxyhemoglobin (30) and diffusion effects (31) were not included.

We believe that the observed underestimation of  $T_1$  and  $T_2$  in the human brain (particularly in WM) even after  $B_1$  correction might be caused by an inhomogeneous intravoxel frequency distribution and multicomponent relaxation (32–37). The presence of different frequencies within a voxel results in asymmetries in the bSSFP signal profile, which have been found and comprehensively studied by Miller et al (38,39). We also observed such asymmetries when we plotted the frequency responses for WM and GM. In the phantom, we did not observe asymmetries, because there are no structures with different frequency components, which can explain a good agreement of the found  $T_1$  and  $T_2$  values with the reference values.

Similar results were found in the work by Nguyen and Bieri (40). Their methodology, named MIRACLE, for  $T_1$  and  $T_2$  mapping is based on frequency-shifted bSSFP scans with subsequent TESS processing for relaxometry. They used a similar experimental setup at 3T and showed a systematic underestimation of  $T_1$  values even after  $B_1$  correction in the brain, while the phantom results were in agreement with the reference. Particularly, they found a 40% underestimation in  $T_1$  for WM and a 20% underestimation of  $T_1$  for GM. They also believe that this is likely due to the asymmetric shape of the bSSFP frequency response in WM and GM due to presence of myelin (35–37). They investigated the effect by characterizing brain tissues with a two-component

relaxation parameter model, as proposed by Miller et al (39) and Deoni et al (41), in which the smaller myelin component had a lower combination of  $T_1$  and  $T_2$  compared with the dominant component. In their simulation, they observed a shift toward lower apparent  $T_1$  values which was in agreement with their experimental results and with the results which we presented in this study.

We believe that the performance and the results of the presented method in the brain deserves further examinations. In addition, further investigation of the in vivo protocol optimization will be the subject of our further research.

The relaxation times  $T_1$  and  $T_2$ , the off-resonance, and the banding free magnitude can be simultaneously and robustly estimated from one dynamic 3D phase-cycled bSSFP sequence. This is an important difference and advantage compared with all existing bSSFP-based techniques for relaxometry purposes.

Such quantitative mapping may be a useful addition to the common techniques for banding artifacts removal that rely on phase-cycling (18). To accomplish this, just a few more additional bSSFP data sets with other RF phase increment settings are required. PLANET may be applied for investigating the local susceptibility and the electrical tissue properties: the off-resonance maps can be used for quantitative susceptibility mapping (QSM) (42). RF phase offset maps, which can be in principle retrieved from Equation [11], could potentially be used for electric properties tomography (43).

Although bSSFP in general is a fast imaging technique with a high SNR efficiency, the disadvantage of using multiple phase-cycled acquisitions is the increased scan duration. In this work, we used 10 steps, but theoretically, considering the number of fitting parameters, the minimum number of required steps is 6. Even though the scan duration is much shorter compared with the duration of the combined 2D gold standard IR-SE and ME-SE and 2D IR-TrueFISP techniques, when 3D coverage is desired, and comparable to that of the combined 3D DESPOT1&2 or 3D TESS technique, we intend to further investigate ways to shorten the scan duration. Shorter acquisition times may be realized by minimizing the number of phase increment steps or by using acceleration techniques, such as compressed sensing (44) or dynamically phase-cycled radial bSSFP (45).

We limited the model to the 3D acquisition mode, assuming a constant FA profile in the slice direction for each voxel. When volumetric coverage is not required, switching to the 2D acquisition mode would considerably decrease the acquisition time, but would lead to a nonideal FA profile over the slice which would compromise the required elliptical behavior of the integrated complex magnetization. An investigation of the feasibility of a 2D approach is subject of our further research.

In this study, we assumed that the chemical shift for all resonances was negligible (i.e., only water resonances present), which indeed was the case for the phantom and the brain experiments. For species with other chemical shifts, such as fat, the model should be adjusted to account for different initial conditions, corresponding to  $\delta_{CS} \neq 0$ .

The method is sensitive to  $B_0$  drift, when it appears while acquiring acquisitions with different phase increment settings. This results in deviations from the single elliptical distribution in the complex plane and errors in the estimated parameters. In our experiments, we did not observe any significant  $B_0$  drift and did not compensate for it. If severe  $B_0$  drift appears, there is a need for correction.

The extension of this work will include a more detailed study of the precision and accuracy of the method in relation to the SNR.

## CONCLUSIONS

We have presented a novel approach, named PLANET, for simultaneous estimation of relaxation times  $T_1$  and  $T_2$  from phase-cycled bSSFP. Prior knowledge about the elliptical signal model was used to reformulate the fitting problem into a convex one, which can be solved directly using a linear least-squares method. The unique ellipse-specific solution of the fitting problem in combination with analytical solutions for  $T_1$  and  $T_2$  make our approach simple, robust and fast, additionally allowing for calculation of the off-resonance and the banding-free magnitude image from the same set of the acquired data.

We have demonstrated that accurate  $T_1$  and  $T_2$  mapping in a phantom as well as in the brain of healthy volunteers is feasible for realistic SNRs and can be performed with a regular coil setup and protocol parameter settings on a clinical MR scanner. We believe that the presented method may be applied in a wide range of applications.

## APPENDIX

### Analytical Solution for Parameters $a$ , $b$ , $M_{\text{eff}}$

The system of nonlinear Equation [9] can be solved for parameters  $a, b, M_{\text{eff}}$  by considering two cases, as illustrated in Supporting Figure S3:  $a > b$  and  $a < b$ , and taking into account the physical constraints for parameters  $a$  and  $b$ :  $0 < a < 1$ ,  $0 < b < 1$ , and the condition of the vertical ellipse:  $A < B$  or  $b < \frac{2a}{1+a^2}$ .

The case  $a = b$ , which from Equation [2] equivalent to  $E_2 = \frac{E_2(1-E_1)(1+\cos\alpha)}{1-E_1\cos\alpha-E_2^2(E_1-\cos\alpha)}$ , and after expanding equivalent to  $\alpha = \cos^{-1}(E_1) = \cos^{-1}\left(\exp\left(-\frac{\text{TR}}{T_1}\right)\right)$ , would lead to a collapse of the ellipse to a line  $x = M_{\text{eff}}$  and should be excluded from consideration by choosing the  $\text{FA} = \alpha \neq \cos^{-1}(E_1)$ .

After solving the Equation [8] using trivial algebraic transformations, the solutions for parameters  $a, b, M_{\text{eff}}$  within interval  $(0,1)$  are:

1. In case  $a > b$ , which is equivalent to  $\alpha > \cos^{-1}(E_1) = \cos^{-1}\left(\exp\left(-\frac{\text{TR}}{T_1}\right)\right)$

$$b_1 = \frac{-x_c A + \sqrt{(x_c A)^2 - (x_c^2 + B^2)(A^2 - B^2)}}{(x_c^2 + B^2)}$$

$$a_1 = \frac{B}{x_c \sqrt{1 - b_1^2} + b_1 B}, \quad M_{\text{eff}1} = \frac{x_c (1 - b_1^2)}{1 - a_1 b_1}$$

2. In case  $a < b$ , which is equivalent to  $\alpha < \cos^{-1}(E_1) = \cos^{-1}\left(\exp\left(-\frac{\text{TR}}{T_1}\right)\right)$

$$b_2 = \frac{x_c A + \sqrt{(x_c A)^2 - (x_c^2 + B^2)(A^2 - B^2)}}{(x_c^2 + B^2)}$$

$$a_2 = \frac{B}{x_c \sqrt{1 - b_2^2} + b_2 B}, \quad M_{\text{eff}2} = \frac{x_c (1 - b_2^2)}{1 - a_2 b_2}$$

To cover the range of  $T_1$  200–2000 ms for the fixed  $\text{TR} = 10$  ms, the FA corresponding to  $a > b$  for all  $T_1$  should be more than  $18^\circ$ , while  $a < b$  area for all  $T_1$  corresponds to FA less than  $5^\circ$ . Therefore, the correct choice of FA should be done by choosing the  $\text{FA} > \cos^{-1}\left(\exp\left(-\frac{\text{TR}}{T_{1 \text{ shortest}}}\right)\right)$ .

## REFERENCES

1. Cheng HL, Stikov N, Ghugre NR, Wright GA. Practical medical applications of quantitative MR relaxometry. *J Magn Reson Imaging* 2012; 36:805–824.
2. Bernstein MA, King KE, Zhou XJ, Fong W. Handbook of MRI pulse sequences. New York: Wiley; 2005.
3. Look DC, Locker DR. Time saving in measurement of NMR and EPR relaxation times. *Rev Sci Instrum* 1970;41:250–251.
4. Christensen KA, Grant DM, Schulman EM, Walling C. Optimal determination of relaxation times of fourier transform nuclear magnetic resonance. Determination of spin-lattice relaxation times in chemically polarized species. *J Phys Chem* 1974;78:1971–1977.
5. Fram EK, Herfkens RJ, Johnson GA, Glover GH, Karis JP, Shimakawa A, Perkins TG, Pelc NJ. Rapid calculation of T1 using variable flip angle gradient refocused imaging. *Magn Reson Imaging* 1987;5:201–208.
6. Homer J, Beevers MS. Driven-equilibrium single-pulse observation of T1 relaxation. A reevaluation of a rapid “new” method for determining NMR spin-lattice relaxation times. *J Magn Reson* 1985;63:287–297.
7. Deoni SCL, Rutt BK, Peters TM. Rapid combined T1 and T2 mapping using gradient recalled acquisition in the steady state. *Magn Reson Med* 2003;49:515–526.
8. Wang HZ, Riederer SJ, Lee JN. Optimizing the precision in T1 relaxation estimation using limited flip angles. *Magn Reson Med* 1987;5: 399–416.
9. Deoni SCL, Peters TM, Rutt BK. Determination of optimal angles for variable nutation proton magnetic spin-lattice, T1, and spin-spin, T2, Relaxation times measurement. *Magn Reson Med* 2004;51:194–199.
10. Wood TC. Improved formulas for the two optimum VFA flip-angles. *Magn Reson Med* 2015;74:1–3.
11. Cheng HLM, Wright GA. Rapid high-resolution T1 mapping by variable flip angles: accurate and precise measurements in the presence of radiofrequency field inhomogeneity. *Magn Reson Med* 2006;55: 566–574.
12. Deoni SCL, Ward HA, Peters TM, Rutt BK. Rapid T2 estimation with phase-cycled variable nutation steady-state free precession. *Magn Reson Med* 2004;52:435–439.
13. Deoni SCL. Transverse relaxation time (T2) mapping in the brain with off-resonance correction using phase-cycled steady-state free precession imaging. *J Magn Reson Imaging* 2009;30:411–417.
14. Preibisch C, Deichmann R. Influence of RF spoiling on the stability and accuracy of T1 mapping based on spoiled FLASH with varying flip angles. *Magn Reson Med* 2009;61:125–135.

15. Yarnykh VL. Optimal radiofrequency and gradient spoiling for improved accuracy of T1 and B1 measurements using fast steady-state techniques. *Magn Reson Med* 2010;63:1610–1626.
16. Schmitt P, Griswold MA, Jakob PM, Kotas M, Gulani V, Flentje M, Haase A. Inversion recovery TrueFISP: quantification of T(1), T(2), and spin density. *Magn Reson Med* 2004;51:661–667.
17. Heule R, Ganter C, Bieri O. Triple echo steady-state (TESS) relaxometry. *Magn Reson Med* 2014;71:230–237.
18. Bangerter NK, Hargreaves BA, Vasanawala SS, Pauly JM, Gold GE, Nishimura DG. Analysis of multiple-acquisition SSFP. *Magn Reson Med* 2004;51:1038–1047.
19. Björk M, Ingle RR, Gudmundson E, Stoica P, Nishimura DG, Barral JK. Parameter estimation approach to banding artifact reduction in balanced steady-state free precession. *Magn Reson Med* 2014;72:880–892.
20. Shcherbakova Y, van den Berg CAT, Lagendijk JJW, Moonen CTW, Bartels LW. Accurate T1 and T2 mapping by direct least-squares ellipse fitting to phase-cycled bSSFP data. In Proceedings of the 24th Annual Meeting of ISMRM, Singapore, 2016. Abstract 0695.
21. Lauzon M, Louis, Frayne R. Analytical characterization of RF phase-cycled balanced steady-state free precession. *Concepts Magn Reson Part A* 2009;34A:133–143.
22. Fitzgibbon AW, Fisher RB, Hill F, Eh E. Direct least squares fitting of ellipses. *IEEE Trans Pattern Anal Mach Intell* 1996;21:1–15.
23. Xiang QS, Hoff MN. Banding artifact removal for bSSFP imaging with an elliptical signal model. *Magn Reson Med* 2014;71:927–933.
24. Hal R, Flusser J. Numerically stable direct least squares fitting of ellipses. *Proc 6th Int Conf Cent Eur Comput Graph Vis* 1998;98:125–132.
25. In den Kleef JJ, Cuppen JJ. RLSQ: T1, T2, and rho calculations, combining ratios and least squares. *Magn Reson Med* 1987;5:513–524.
26. Yarnykh VL. Actual flip-angle imaging in the pulsed steady state: a method for rapid three-dimensional mapping of the transmitted radiofrequency field. *Magn Reson Med* 2007;57:192–200.
27. Bieri O, Scheffler K. Optimized balanced steady-state free precession magnetization transfer imaging. *Magn Reson Med* 2007;58:511–518.
28. Bieri O, Markl M, Scheffler K. Analysis and compensation of eddy currents in balanced SSFP. *Magn Reson Med* 2005;54:129–137.
29. Warntjes JBM, Dahlqvist Leinhard O, West J, Lundberg P. Rapid magnetic resonance quantification on the brain: optimization for clinical usage. *Magn Reson Med* 2008;60:320–329.
30. Dharmakumar R, Hong J, Brittain JH, Plewes DB, Wright GA. Oxygen-sensitive contrast in blood for steady-state free precession imaging. *Magn Reson Med* 2005;53:574–583.
31. Bieri O, Scheffler K. Effect of diffusion in inhomogeneous magnetic fields on balanced steady-state free precession. *NMR Biomed* 2007;20:1–10.
32. Lancaster JL, Andrews T, Hardies LJ, Dodd S, Fox PT. Three-pool model of white matter. *J Magn Reson Imaging* 2003;17:1–10.
33. Laule C, Vavasour IM, Moore GRW, Oger J, Li DKB, Paty DW, MacKay AL. Water content and myelin water fraction in multiple sclerosis. A T2 relaxation study. *J Neurol* 2004;251:284–293.
34. Lee J, Shmueli K, Fukunaga M, van Gelderen P, Merkle H, Silva AC, Duyn JH. Sensitivity of MRI resonance frequency to the orientation of brain tissue microstructure. *Proc Natl Acad Sci U S A* 2010;107:5130–5135.
35. van Gelderen P, de Zwart JA, Lee J, Sati P, Reich DS, Duyn JH. Nonexponential T<sub>2</sub> decay in white matter. *Magn Reson Med* 2012;67:110–117.
36. Lee J, Shmueli K, Kang BT, Yao B, Fukunaga M, Van Gelderen P, Palumbo S, Bosetti F, Silva AC, Duyn JH. The contribution of myelin to magnetic susceptibility-weighted contrasts in high-field MRI of the brain. *Neuroimage* 2012;59:3967–3975.
37. van Gelderen P, Jiang X, Duyn JH. Effects of magnetization transfer on T1 contrast in human brain white matter. *Neuroimage* 2016;128:85–95.
38. Miller KL. Asymmetries of the balanced SSFP profile. Part I: theory and observation. *Magn Reson Med* 2010;63:385–395.
39. Miller KL, Smith SM, Jezzard P. Asymmetries of the balanced SSFP profile. Part II: white matter. *Magn Reson Med* 2010;63:396–406.
40. Nguyen D, Bieri O. Motion-insensitive rapid configuration relaxometry. *Magn Reson Med* 2017;78:518–526.
41. Deoni SCL, Rutt BK, Arun T, Pierpaoli C, Jones DK. Gleaning multi-component T1 and T2 information from steady-state imaging data. *Magn Reson Med* 2008;60:1372–1387.
42. Wang Y, Liu T. Quantitative susceptibility mapping (QSM): decoding MRI data for a tissue magnetic biomarker. *Magn Reson Med* 2015;73:82–101.
43. Katscher U, Voigt T, Findekklee C, Vernickel P, Nehrke K, Dössel O. Determination of electric conductivity and local SAR via B1 mapping. *IEEE Trans Med Imaging* 2009;28:1365–1374.
44. Cukur T. Accelerated phase-cycled SSFP imaging with compressed sensing. *IEEE Trans. Med. Imaging* 2015;34:107–115.
45. Benkert T, Eheses P, Blaimer M, Jakob PM, Breuer FA. Dynamically phase-cycled radial balanced SSFP imaging for efficient banding removal. *Magn Reson Med* 2015;73:182–194.

## SUPPORTING INFORMATION

Additional Supporting Information may be found in the online version of this article.

**Fig. S1.** Experimental results from the MT study: (a) the banding free effective magnitude images, calculated for the default and long RF pulses; (b) T<sub>1</sub> maps calculated for the default and long RF pulses; (c) T<sub>2</sub> maps calculated for the default and long RF pulses; (d) the Signal Ratio and MTR calculated for the default RF pulse compared with the long RF pulse. The duration of the default RF pulse was 0.84 ms. The duration of long RF pulse was 2.86 ms.

**Fig. S2.** SNR maps calculated for one axial slice of the brain (a) and the phantom (b).

**Fig. S3.** Geometrical representation of the parameter space for a and b. The white area corresponds to the vertical ellipse for cases a > b and a < b, and the black area corresponds to the horizontal ellipse.

**Table S1.** The quantitative results from three ROIs placed in white matter for the default and long RF excitation pulses.